Arabian Journal of Geosciences (2018) 11: 311
https://doi.org/10.1007/s12517-018-3635-y

ORIGINAL PAPER

Identification of metamorphic rocks in Wuliangshan Mountains (Southwest China) using ASTER data

Qi Chen[1,2] · Zhifang Zhao[2] · Qigang Jiang[1] · Shucheng Tan[2] · Yinggui Tian[3]

Received: 13 March 2018 / Accepted: 29 May 2018 / Published online: 21 June 2018

Abstract

Metamorphic rocks have scientific significance for parsing the evolutionary process of an orogenic belt. The Wuliangshan area is a very complex region of metamorphism, where it is nearly impossible to conduct conventional geological investigation because of the extremely rugged topography and difficult travel conditions. Previous research on the area's metamorphic rocks is limited. There are two metamorphic belts, the Yunling-Jinghong and Wuliangshan metamorphic belts, identified by means of traditional field survey. To better identify the metamorphic rocks of the Wuliangshan area, this study adopted the principal component analysis (PCA) and spectrum-area (S-A) methods, using Advanced Spaceborne Thermal Emission and Reflection Radiometer (ASTER) data, to extract the anomalies of diagnostic metamorphic minerals in metamorphic rocks, such as actinolite, chlorite, epidote, biotite, muscovite, hornblende, andalusite, staurolite, cordierite, and sillimanite. The methods are based on the principle that the metamorphic degree is reflected by the diagnostic metamorphic minerals. Profile investigation and petrographic analysis show that the identification accuracy of the diagnostic metamorphic minerals reached 85.65%. Seven concentrations of metamorphic rocks were delineated based on the extracted metamorphic mineral anomalies. Compared with previous study results, this study showed that there are metamorphic rocks in defined Regions 1, 2, 3, 4 and 6, which are consistent with existing data; whereas in Regions 5 and 7, there is new information regarding the existence of metamorphic rocks, which may offer new clues about the formation of this area through additional studies. The results of this study not only reveal detailed information for geological survey of the Wuliangshan area but also provide useful methods for future surveys.

Keywords Metamorphic rock identification · Metamorphic minerals · ASTER · Wuliangshan · China

✉ Zhifang Zhao
zzf_1002@163.com

Qi Chen
ynu_cq@163.com

Qigang Jiang
jiangqigang@qq.com

Shucheng Tan
695602890@qq.com

Yinggui Tian
437348841@qq.com

[1] College of Geoexploration Science and Technology, Jilin University, Changchun, China

[2] College of Resource Environment and Earth Sciences, Yunnan University, Kunming, China

[3] Institute of Yunnan Geological Mineral Exploration, Kunming, China

Introduction

Geological mapping is the basis of geological study. Because structure-fluid magmatism and potential metallogenesis are often concentrated in metamorphic rock areas, metamorphic rocks are of scientific significance and can provide evidence for parsing the evolutionary process of orogenic belts, wherein geological mapping is even more important (Fry 1984). To conduct geological mapping in metamorphic rock areas, it is necessary to obtain the distribution of metamorphic rocks and their metamorphic degrees. Geologists have already completed considerable research on metamorphic rocks. For example, Spalla et al. (2002) used regional-scale correlation of the structural and metamorphic succession of events to identify the crustal portions recording coherent thermal and tectonic evolution; Aoki et al. (2011) recognized the Shimanto HP metamorphic belt within the traditional Sanbagawa HP metamorphic belt in SW Japan using high-precision analytical equipment to provide more precise age constraints for

accretion and metamorphism of geological units; and Kakar et al. (2015) presented the petrology and geochemistry of the dominant lithologies, such as garnetiferous amphibolites, amphibolites, and greenschists, from the metamorphic sole of the Muslim Bagh ophiolite (Pakistan) to determine their protolith and the type of tectonic setting in which they formed. Additionally, Philippon et al. (2015) used 3D modeling to characterize post-foliation deformation in metamorphic terrains (Syros, Cyclades, and Greece).

The minerals of metamorphic rocks contain inherited minerals (quartz, orthoclase, anorthose, etc.) and metamorphic minerals (epidote, andalusite, staurolite, etc.). The inherited minerals are the original minerals in the rock, while the metamorphic minerals formed during the complex process of metamorphism. The diagnostic metamorphic minerals represent the type of metamorphism that occurred, as they have a stable range indicating metamorphic conditions (temperature, pressure, and sometimes the composition of original rock). For example, epidote, chlorite, actinolite, muscovite, and biotite form during low-grade metamorphism and indicate that metamorphic conditions were of low temperature and pressure; hornblende, andalusite, staurolite, and cordierite form during medium-grade metamorphism and indicate that metamorphic conditions were of medium temperature and pressure; and sillimanite forms during high-grade metamorphism and indicates that metamorphic conditions were of high temperature and high pressure. Therefore, these diagnostic metamorphic minerals can be good indicators of the distribution of metamorphic rocks and their metamorphic degrees.

The Wuliangshan area is rich in complex metamorphic rocks. Xue (1988) proposed that the metamorphism is of a regional dynamothermal metamorphic type. Hou et al. (2013) thought that the metamorphic belt is a progressive metamorphic zone and has the characteristics of inhomogeneity and uncontinuative isograde, which is different from regional metamorphism of homogeneity and isograde. Initially, the study area was classified as the Wuliangshan metamorphic belt (Genyao and Jiaju 1996). As research progressed, the area was roughly divided into two metamorphic belts (Yunnan Geological Mineral Bureau, 1990). Until now, there has been no more literature published on the further subdivision of metamorphic belts in the Wuliangshan area because of the extremely rugged topography and difficult travel conditions. Therefore, further subdivision of the metamorphic rocks needed to be completed, which can be obtained from information on the diagnostic metamorphic minerals.

Remote sensing techniques have been widely and successfully used for geological applications, such as alteration mapping, lithological discrimination, and mineral detection (Ferrier et al. 2002; Gabr et al. 2015; Kratt et al. 2010; Meer et al. 2012; Rowan et al. 1977; Sabins 1999; Zoheir and Emam 2014). The multifractal theory (Cheng 1999) has been successfully used to recognize weak but complex geochemical anomalies in areas covered by deserts, regolith, or vegetation. Various successful case studies using multifractal models for processing geochemical data have been reported (Agterberg 2014; Agterberg 2012; Cao and Cheng 2012; Carranza 2009; Carranza 2010; Chen and Cheng 2016; Cheng 2007; Cheng 2008; Cheng 2012; Cheng and Agterberg 1996; Cheng and Agterberg 2009; Cheng et al. 1994; Cheng et al. 2010; Cheng et al. 1999; Cheng et al. 2000; Li et al. 2003; Lima et al. 2003a; Lima et al. 2008; Lima et al. 2003b; Liu et al. 2017; Wang et al. 2012; Xu and Cheng 2001; Zuo et al. 2012; Zuo et al. 2013a; Zuo et al. 2013b). Based on the same principle, the multifractal theory is also introduced in the remote sensing data processing in this study.

As the Advanced Spaceborne Thermal Emission and Reflection Radiometer (ASTER) data contain the spectral characteristics of minerals, this principal component analysis (PCA) and spectrum-area (S-A) methods, based on multifractal theory, were adopted to identify metamorphic minerals, such as actinolite, chlorite, epidote, biotite, muscovite, hornblende, andalusite, staurolite, cordierite, and sillimanite with the ASTER data in the Wuliangshan area. Furthermore, to better identify the metamorphic rocks of the Wuliangshan area, the extracted metamorphic mineral anomalies were used to analyze the distribution of metamorphic rocks and compared with the previous studies.

Geological setting

The study area is in western Yunnan Province, China, in the Simao Basin in the middle of the Sanjiang orogenic belt (BaoLong et al. 2008; JunLai et al. 2006; Wang et al. 2015). The latitude and longitude coordinates of the study area are 100° 30′ 00″ E–100° 45′ 00″ E and 24° 20′ 00″–24° 40′ 00″ N respectively and the area covers 900 km^2. With a high altitude, extremely rugged topography and difficult travel conditions, in which the highest altitude is 3306 m and most slopes are greater than 35°, it is almost impossible to conduct conventional geological investigation in this area (Fig. 1).

According to the regional geological background, there are relatively complete formation outcrops in the study area, which span from the Palaeoproterozoic era to the Cenozoic era. The main strata are the Palaeozoic Wuliangshan (P*zw.*) and Daxinshan Formations (Pz$_2$*dx.*); the Triassic Manghuai (T$_2$*m*), Sanhedong (T$_3$*sh*), Waluba (T$_3$*wl*), and Maichuqing Formations (T$_3$*m*); the Triassic–Jurassic Xiaodingxi Formation (TJ*xd1*); the Jurassic Yangjiang (J$_1$*y*), Huakaizuo (J$_1$*h*), and Bazhulu Formations (J$_1$*b*); the Cretaceous Jingxing (K$_1$*j*) and Nanxin Formations (K$_1$*n*); the Neogene Pliocene Sanying Formation (N$_2$*s*); and Quatemary–Holocene sediment (Q*h*). The Palaeozoic Wuliangshan Formation (P*zw.*) is

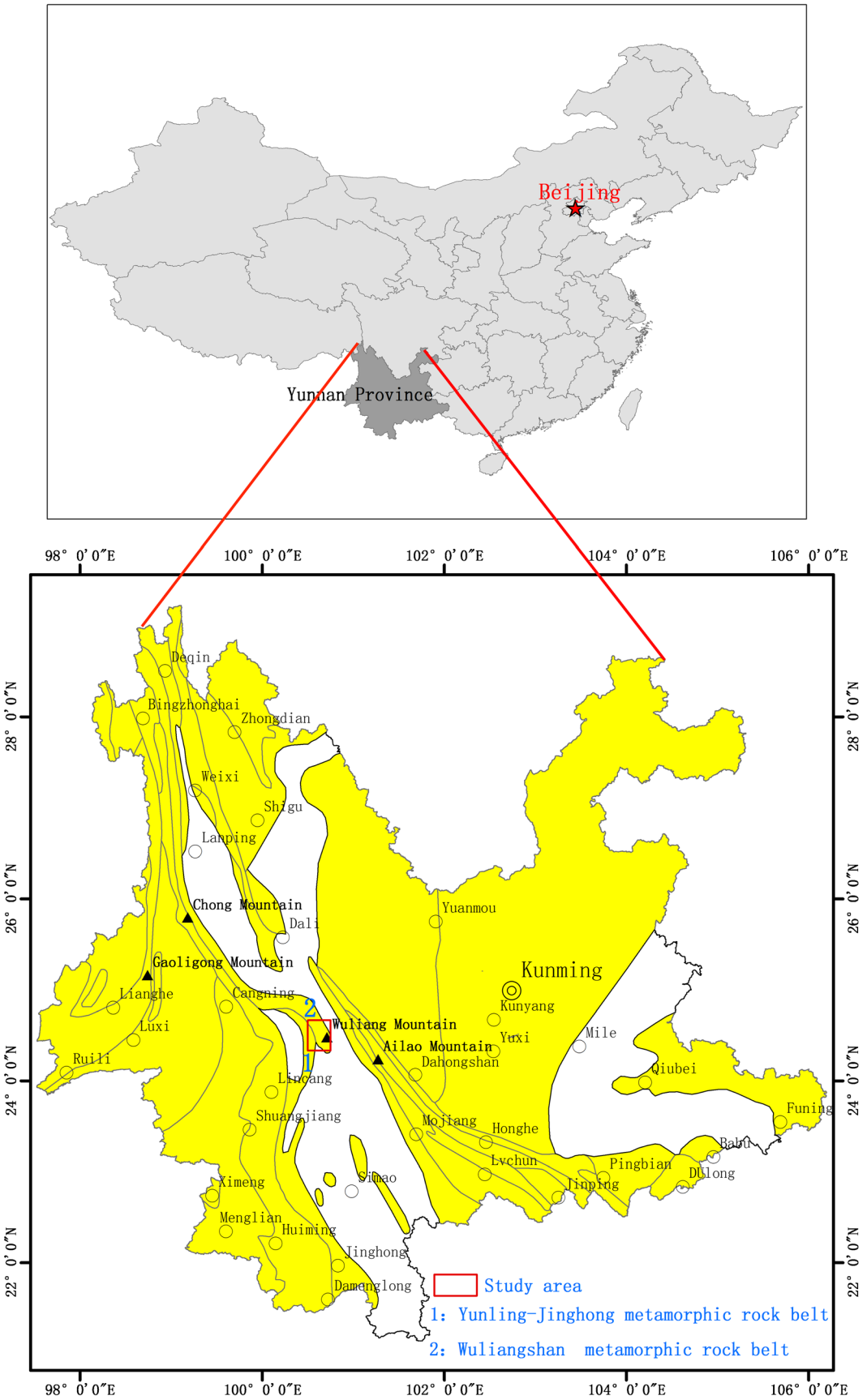

Fig. 1 Map of the study area (Yunnan Geological Mineral Bureau, 1990)

in the central part of the study area; the Palaeozoic Daxinshan Formation ($Pz_2dx.$), the Triassic–Jurassic Xiandingxi Formation ($TJxd^l$) and Quatemary–Holocene sediment (Qh) are in the southwest part of the study area; the Triassic Manghuai = (T_2 m), Sanhedong (T_3sh), Waluba = (T_3wl), and Maichuqing Formations (T_3m); the Jurassic Yangjiang (J_1y), Huakaizuo (J_1h), and Bazhulu Formations (J_1b); the Cretaceous Jingxing (K_1j) and Nanxin Formations (K_1n); and the Neogene–Pliocene Sanying Formation (N_2s) are in the northeast part of the study area. The distribution of these strata are controlled by NW-trending faults (Fig. 2).

The Palaeozoic Daxinshan Formation ($Pz_2dx.$) and the Wuliangshan Formation ($Pzw.$) have a high concentration of metamorphic minerals. Two metamorphic belts were defined in previous study according to metamorphic characteristics and metamorphic types. These are the Yunling-Jinghong metamorphic belt and the Wuliangshan metamorphic belt (Yunnan Geological Mineral Bureau, 1990). Detailed information regarding the metamorphic belts is listed as follows:

The Yunling-Jinghong metamorphic belt

This metamorphic belt is distributed on both sides of the Lancang River in a NW-trending direction. The metamorphic strata include the upper Palaeozoic Daxinshan Formation ($Pz_2dx.$). The lower segment lithology combination is ash and grey-black sericitic slate, and the upper segment is slate and sandy slate, which is 220–850 m thick. The metamorphic mineral assemblage is composed of sericite and chlorite, and the metamorphic degree is low greenschist facies. The metamorphic period is the end of the Variscan orogeny (Fig. 3a).

The Wuliangshan metamorphic belt

This metamorphic belt is near the eastern part of the Lancang River in a NW-trending direction. The metamorphic strata include the Palaeozoic Wuliangshan Formation. The Palaeozoic Wuliangshan Formation is divided into four members ($Pz_1W.^1$, $Pz_1W.^2$, $Pz_2W.^3$, and $Pz_2W.^4$) according to the lithologic characteristics and metamorphic degree.

$Pz_1W.^1$: The lithology consists of grey and dark grey biotite plagioclase granulite, staurolite two-mica schist, and two-mica quartz schist, with a thickness of 824.9–850.5 m (Fig. 3b).

$Pz_1W.^2$: The lithology consists of grey and grey-white biotite quartzite, two-mica quartzite, epidote biotite plagioclase granulite, and two-mica quartz schist, with a thickness of 1025.4–1261.3 m (Fig. 3c).

$Pz_2W.^3$: The lithology consists of grey greisenized epidote biotite plagioclase granulite, two-mica quartz schist, and muscovite schist, with a thickness of 692.7–747.5 m (Fig. 3d).

$Pz_2W.^4$: The lithology consists of grey to light grey muscovite quartzite, biotite quartzite, epidote quartzite, and two-mica quartz schist, with a thickness of 481.5–770.4 m (Fig. 3e).

The main metamorphic minerals of $Pz_1W.^1$ and $Pz_1W.^2$ are muscovite, biotite, chlorite, epidote, andalusite, cordierite, staurolite, and kyanite, and the metamorphic degree is generally high greenschist facies-low amphibolite facies. The main metamorphic minerals of $Pz_2W.^3$ and $Pz_2W.^4$ are muscovite, biotite, chlorite, and epidote, and the metamorphic degree is low greenschist facies.

Methods

Data acquisition and processing

Advanced Spaceborne Thermal Emission and Reflection Radiometer (ASTER) is a multispectral imaging sensor on board the Terra satellite, which was launched on December 18, 1999, as part of NASA's Earth Observing System program. It can measure reflected and emitted electromagnetic radiation from the Earth's surface and atmosphere in 14 bands. There are three groups of bands: (i) three recording visible and near infrared (VNIR) bands ranging from 0.52 to 0.86 μm at a spatial resolution of 15 m; (ii) six recording portions of shortwave infrared (SWIR) bands from 1.6 to 2.43 μm at a spatial resolution of 30 m; and (iii) five recording thermal infrared (TIR) bands from 8.125 to 11.65 μm at a spatial resolution of 90 m. The ASTER swath width is 60 km (each scene is 60 × 60 km) (Table 1).

Two scenes of ASTER image data were acquired in this study with good quality and minimal cloud coverage. The acquisition dates were February 23, 2002, and February 2, 2006.

In this study, the ENVI® 5.3 and ArcGIS®10.3 software packages were used to process the ASTER images. The main processing of the ASTER data included atmospheric correction (Perkins et al., 2005; Nguyen et al., 2015; Rani et al., 2017), data re-sampling, layer stacking, and geometric correction. Figure 4 shows the final image, with a combination of bands 7, 3 N, and 1 after data processing.

Analysis of metamorphic mineral spectral response using ASTER data

The minerals' spectral response features are the basis for mineral extraction. Epidote was used as an example to analyze the mineral spectral response features in the ASTER data as follows:

The spectral curve of epidote in the ASTER data is shown in Figs. 5 and 6. The spectral response of epidote is reflected

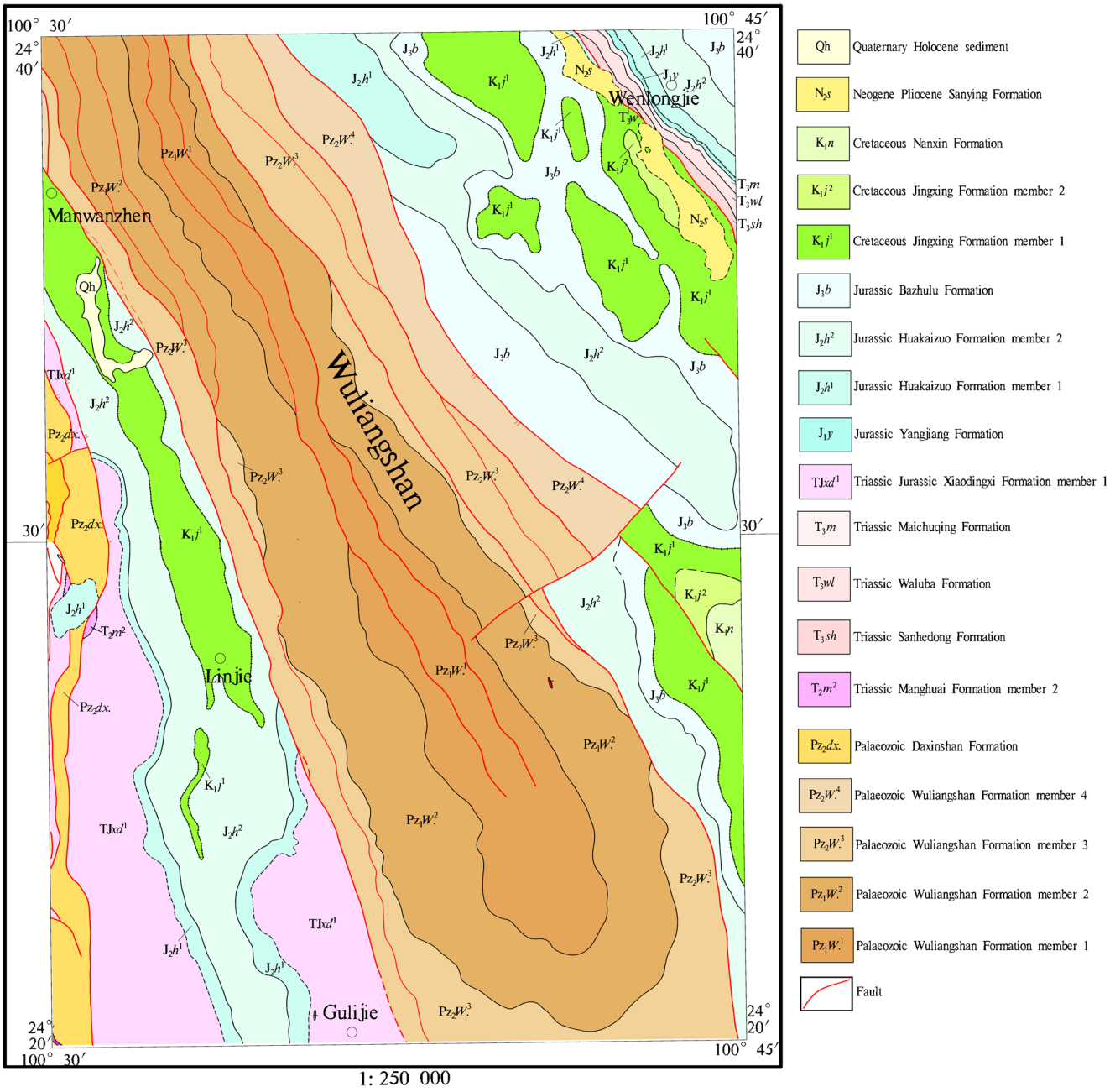

Fig. 2 Geological map of the study area

as absorption valleys in Bands 8 (B8) and 12 (B12) and strong reflections in Bands 5 (B5) and 9 (B9). Therefore, ASTER Bands 5, 8, 9, and 12 can be taken as epidote characteristic spectra. In this manner, the characteristic spectra of other metamorphic minerals can be summarized as follows: ASTER Bands 1,2, 9, and 13 are the characteristic spectra of chlorite; ASTER Bands 1, 8, 10, and 12 are the characteristic spectra of biotite; ASTER Bands 6, 9, 12, and 13 are the characteristic spectra of muscovite; ASTER Bands 7, 8, 10, and 11 are the characteristic spectra of hornblende; ASTER Bands 1, 5, 11, and 12 are the characteristic spectra of andalusite; ASTER Bands 1, 2, 11, and 14 are the characteristic spectra of staurolite; ASTER Bands 2, 6, 11, and 12 are the characteristic spectra of cordierite; ASTER Bands 3, 4, 11, and 12 are the characteristic spectra of actinolite; and ASTER Bands 5, 7, 10, and 11 are the characteristic spectra of sillimanite (Table 3).

Extraction of metamorphic mineral anomalies

The principle component analysis (PCA) and spectrum-area (S-A) methods were used to extract the metamorphic mineral anomalies.

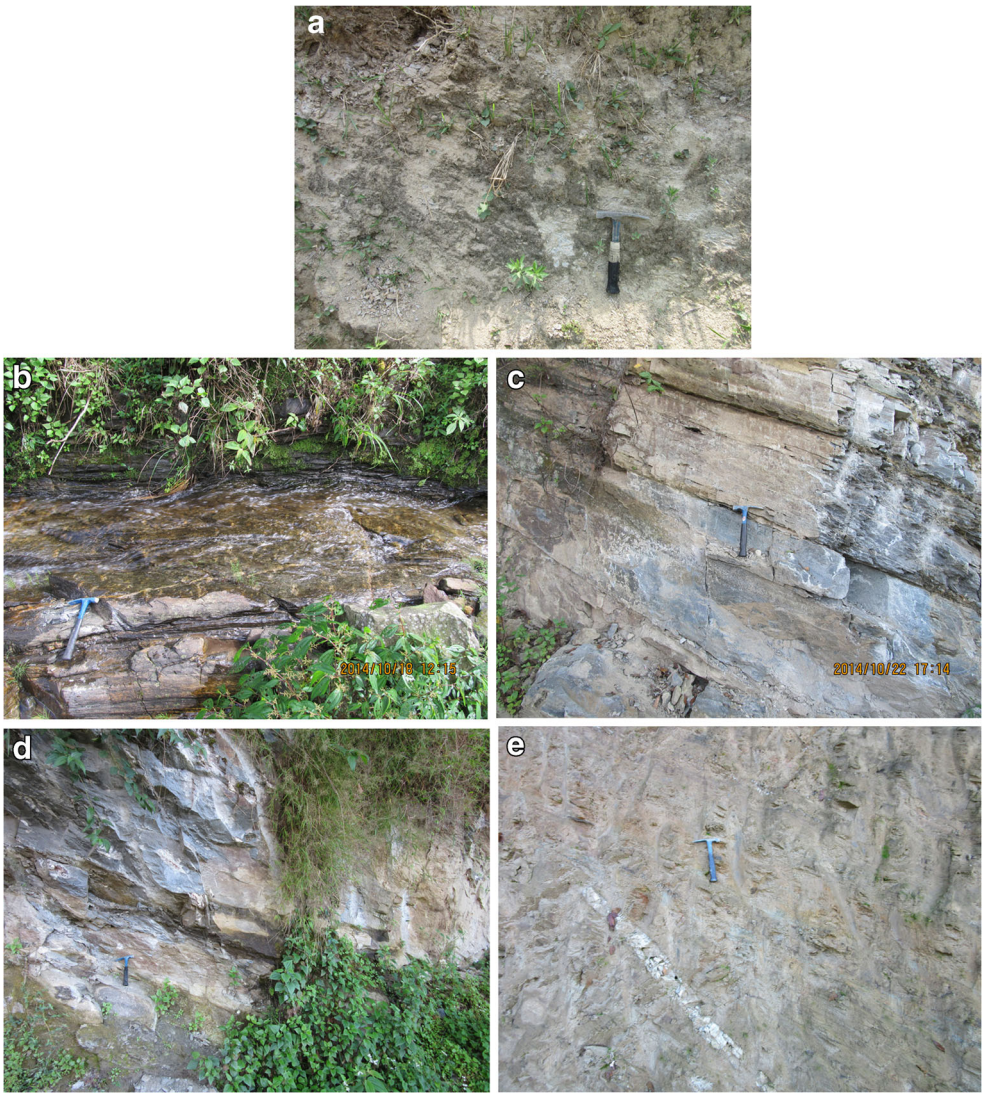

Fig. 3 **a** Interbedding of purple grey silty slate and argillic slate ($Pz_2dx.$). **b** Biotite plagioclase granulite ($Pz_1W.^1$). **c** Interbedding of grey-white layered biotite quartzite and grey two-mica quartz schist ($Pz_1W.^2$). **d** Interbedding of grey greisenized epidote biotite plagioclase granulite and grey muscovite schist ($Pz_1W.^3$). **e** Interbedding of striated muscovite quartzite and greyish green two-mica quartz schist ($Pz_1W.^4$)

Principle component analysis

Images generated by digital data from various wavelength bands often appear similar and convey essentially the same information (Arnous and Sultan, 2014). The principle component analysis (PCA) method is typically applied to enhance information extraction in remote sensing data processing, which is based on the statistical characteristics of images as

Table 1 Spectral characteristics and wavelength ranges of ASTER data

Characteristics	VNIR	Wavelength range (μm)	SWIR	Wavelength range (μm)	TIR	Wavelength range (μm)
Band and wavelength range (μm)	1	0.52–0.60	4	1.60–1.70	10	8.125–8.475
	2	0.63–0.69	5	2.145–2.18	11	8.475–8.825
	3 N	0.78–0.86	6	2.185–2.225	12	8.925–9.27
	3B	0.78–0.8	7	2.235–2.285	13	10.25–10.95
			8	2.295–2.36	14	10.95–11.6
			9	2.36–2.43		
Spatial resolution (m)		15		30		90
Swath width (km)		60		60		60
Signal quantization level (bits)		8		8		12

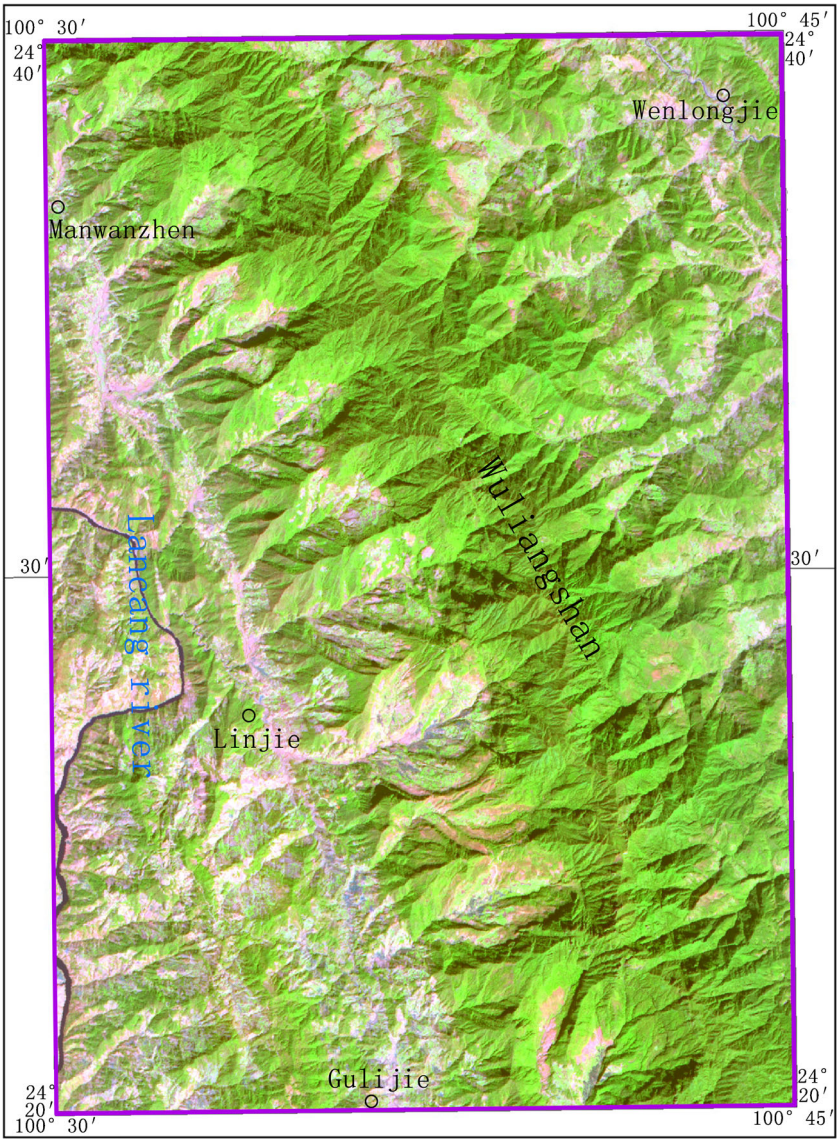

Fig. 4 ASTER image of the study area with combination of R (Band 7), G (Band 3 N), B (Band 1)

shown in Formula (1) via multi-dimensional orthogonal linear transformation. After the transformation, the linear combination of the original image is generated as a new set of components.

$$Y = AX \tag{1}$$

In Formula (1), X represents the multispectral vectors before the PCA transformation, Y represents the principal components after the PCA transformation, and A represents the transformation matrix, which is the eigenvector matrix of the covariances of X.

The 10 analyzed characteristic spectra of the metamorphic minerals in the ASTER Bands were processed using principal component analysis to concentrate the information of metamorphic mineral anomalies into a single PC.

The PCA method was adopted for the epidote remote sensing anomalies as follows:

The ASTER Bands 5, 8, 9, and 12 were used in the PCA transformation based on the spectral properties listed above, and PCs (principal components) representing the epidote remote sensing anomalies should have the characteristics that obtain positive contributions from ASTER Bands 5 and 9 and negative contributions from ASTER Bands 8 and 12. Thus, the PC4 was determined to represent the epidote remote sensing anomalies PC (Table 2).In the same principle, Table 3 shows the parameters of the characteristic spectra and principle components of the other nine metamorphic minerals for anomaly extraction.

Spectrum-area

Multifractal theory is effectively applied in the enhanced extraction of weak mineralization minerals and is based on the principle of generalized self-similarity and local

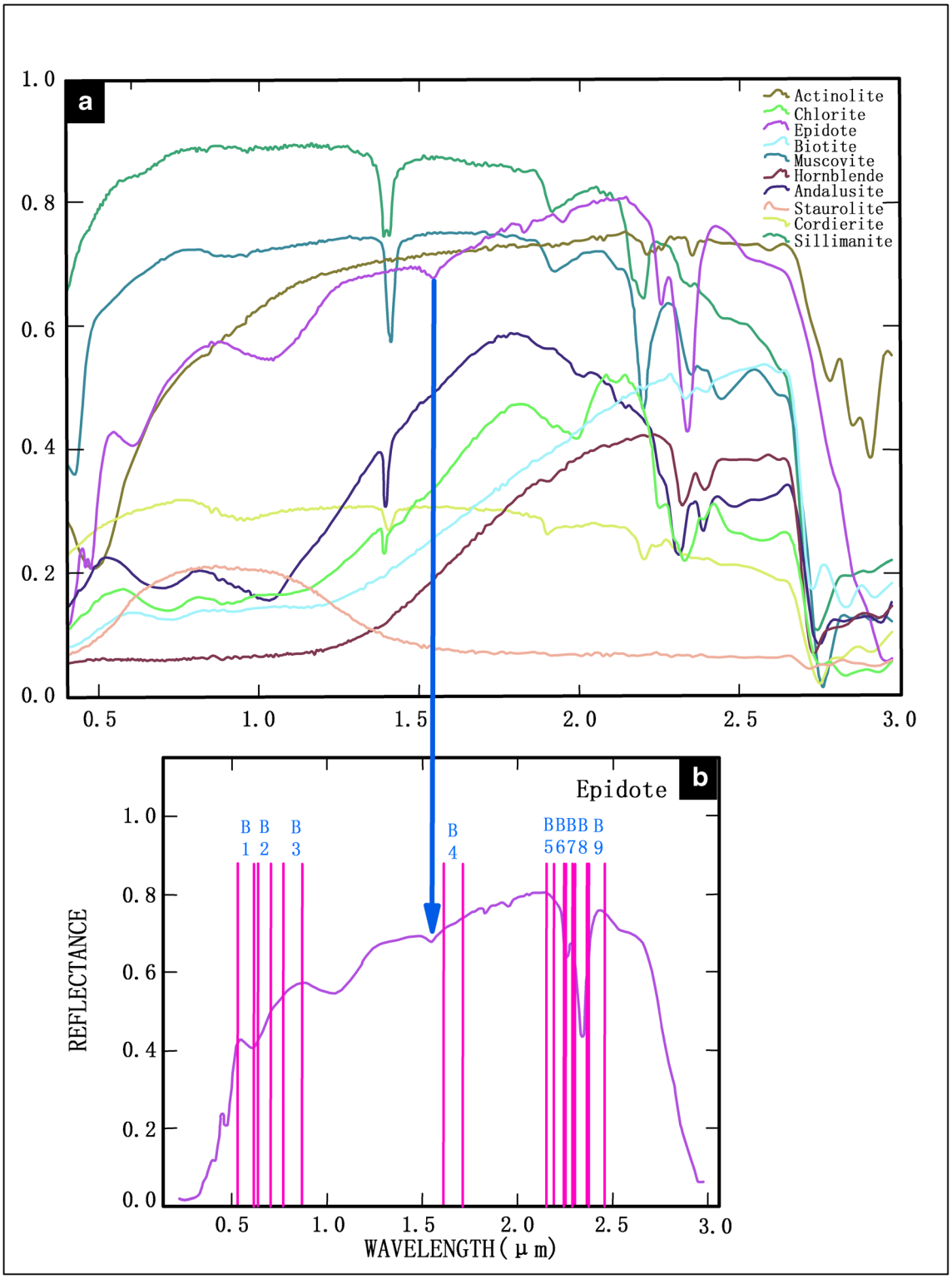

Fig. 5 Spectral curves of metamorphic minerals from the visible to shortwave infrared spectrum in ASTER Bands 1–9: **a** Spectral curves of ten metamorphic minerals from the United States Geological Survey (USGS). **b** Spectral curve of epidote in ASTER Bands 1–9

singularity. The spectrum-area (S-A) method, which is taken as the typical application of the multifractal theory, can separate weak mineralization anomalies from the geological background (Cheng et al. 1994, Cheng and Agterberg, 1996, Cheng et al., 1999, 2000, Cheng, 2012). The S-A method measures anisotropic generalized self-similarity in the Fourier spectrum space and identifies different generalized self-similarities of the energy spectra distribution by

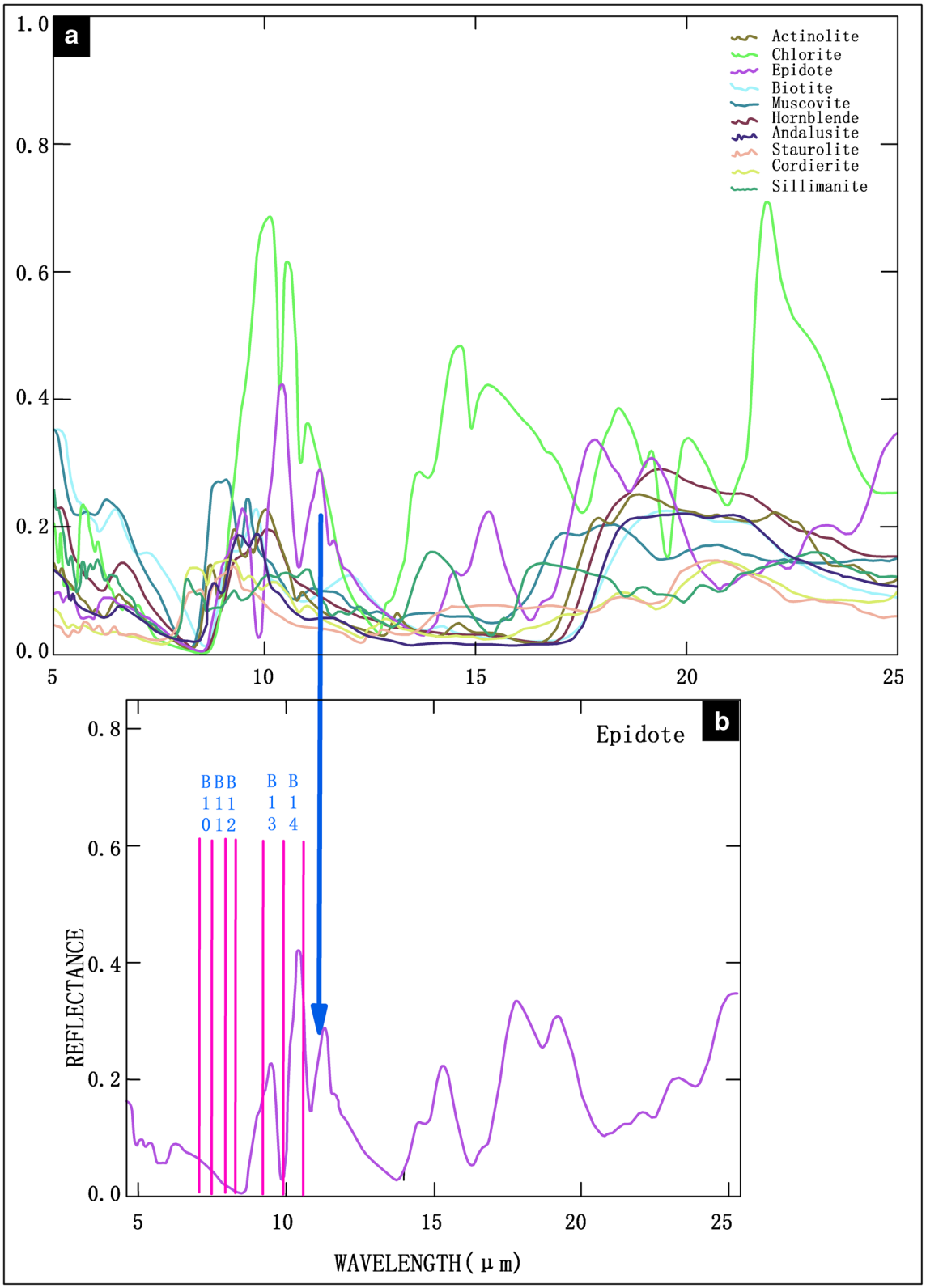

Fig. 6 Spectral curves of metamorphic minerals in the thermal infrared wave infrared spectrum in ASTER Bands 10–14: **a** Spectral curves of ten metamorphic minerals from the United States Geological Survey (USGS). **b** Spectral curve of epidote in ASTER Bands 10–14

which the background and anomalies can be divided into different filters.

Self-similarity can be expressed using the following formula:

Table 2 Contributions of principal component of epidote from ASTER bands

	Band5	Band8	Band9	Band12
PC1	0.587863	0.590669	0.547961	0.072563
PC2	0.564701	− 0.693485	0.083504	0.439566
PC3	0.516946	0.251259	− 0.810367	− 0.113764
PC4	0.261336	− 0.327196	0.189927	− 0.888017

$$A(>S)\propto S^{-\beta} \quad (2)$$

In Formula (2), S is the spectral energy density, and A is the area of the spectral energy density greater than a certain critical value (S_0). β is available in the log A ($>S_0$) – log (S) diagram. All straight segments usually obey this formula in the log-log diagram. Different straight segments correspond to different fractal relationships, with the intersection of two straight spectral density lines representing the threshold of the fractal filter. A number of abnormal filter models can be produced according to the threshold value, by which the Fourier inverse transformation is used to separate mineral anomalies from the background.

The S-A method was used to obtain the epidote anomalies as follows: the Fourier transformation was applied to transfer the epidote anomalies PC(PC4) from the space domain to the frequency domain at the beginning, and the log-log diagram between the frequency (S) and number of pixels (A) in PC4 was generated in the frequency domain (Fig. 7a). Based on the log-log fractal characteristics diagram in the frequency domain space, the straight segment was then adopted to represent different fractal characteristics for the background and the epidote remote sensing anomalies. That is, the fractal filter threshold, demonstrated by the intersection of the two straight lines of the spectral density values, could be obtained. In the log-log diagram of the epidote remote sensing anomalies, the fractal filter threshold was 1.4, which was determined to distinguish the epidote remote sensing anomalies from the geological background. Accordingly, the filter model was designed as Fig. 7b, in which the black area represents the geological background and the green area represents the epidote anomalies. In the same principle, Table 3 shows the parameters of the S-A fractal filters (threshold value) in the other nine metamorphic mineral anomaly extractions.

Profile investigation and petrographic analysis

The identification of the aforementioned extracted metamorphic mineral anomalies was determined through profile investigation in the field and sample petrographic analysis using a microscope.

Profile investigation

The profile investigation should choose areas with complete formation, good outcrops, and simple structure. The profile investigation contains GPS locations, lithologic identification, sample collection, photography, and thin section production. Two profiles (PM28, PM33) were carefully investigated in this study.

PM28: This profile was investigated from April 18 to 20, 2014. The profile length was 4949 m, in which 61 layers were identified, 94 samples were collected, 62 photos were taken, and 94 thin sections were produced.

PM33: This profile was investigated from October 12 to 15, 2014. The profile length was 8061 m, in which 106 layers were identified, 122 samples were collected, 108 photos were taken, and 122 thin sections were produced.

Table 3 The characteristic spectra, anomaly principle components, and S-A fractal filters (threshold value) in ten metamorphic mineral anomaly extractions

Minerals	Characteristic spectrum (PCA Bands)	Principle component	S-A fractal filter (threshold value of log (DN) in the log-log diagram)
Chlorite	B1, B2, B9, B13	PC4	1.6
Epidote	B5, B8, B9, B12	PC4	1.4
Biotite	B1, B8, B10, B12	PC3	1.5
Muscovite	B6, B9, B12, B13	PC4	1.1
Hornblende	B7, B8, B10, B11	PC2	1.3
Andalusite	B1, B5, B11, B12	PC2	1.6
Staurolite	B1, B2, B11, B14	PC4	1.5
Cordierite	B2, B6, B11, B12	PC3	1.2
Actinolite	B3, B4, B11, B12	PC3	1.7
Sillimanite	B5, B7, B10, B11	PC4	1.1

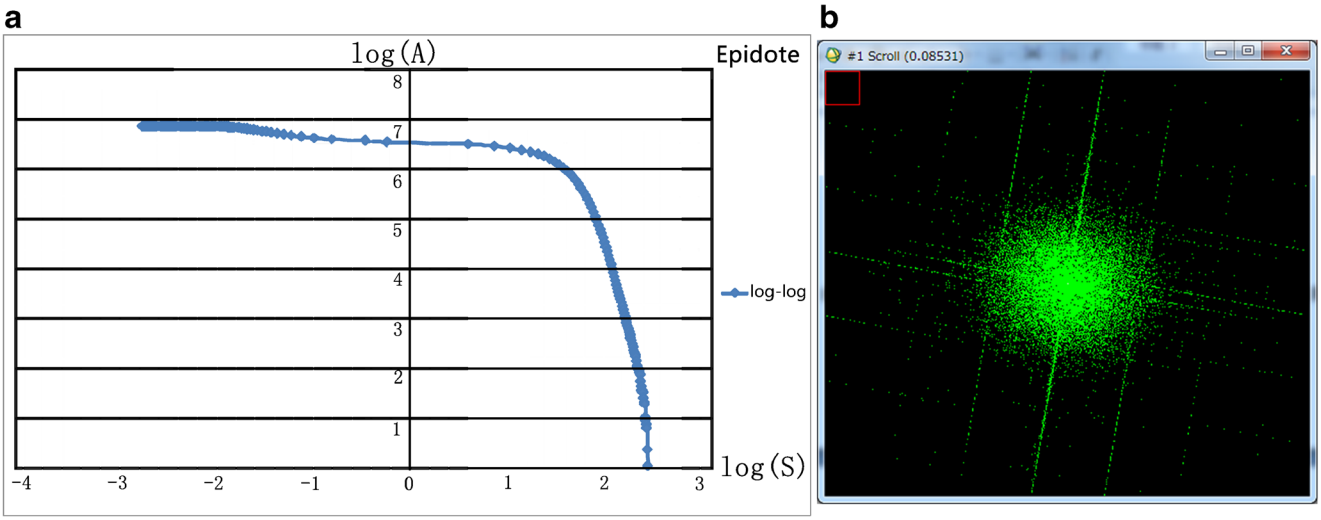

Fig. 7 Extraction of epidote remote sensing anomalies with PC4 by S-A method. **a** Log(S)-log(A) diagram of the epidote remote sensing anomalies in the frequency domain. **b** Fractal filter of the epidote remote sensing anomalies from the geological background

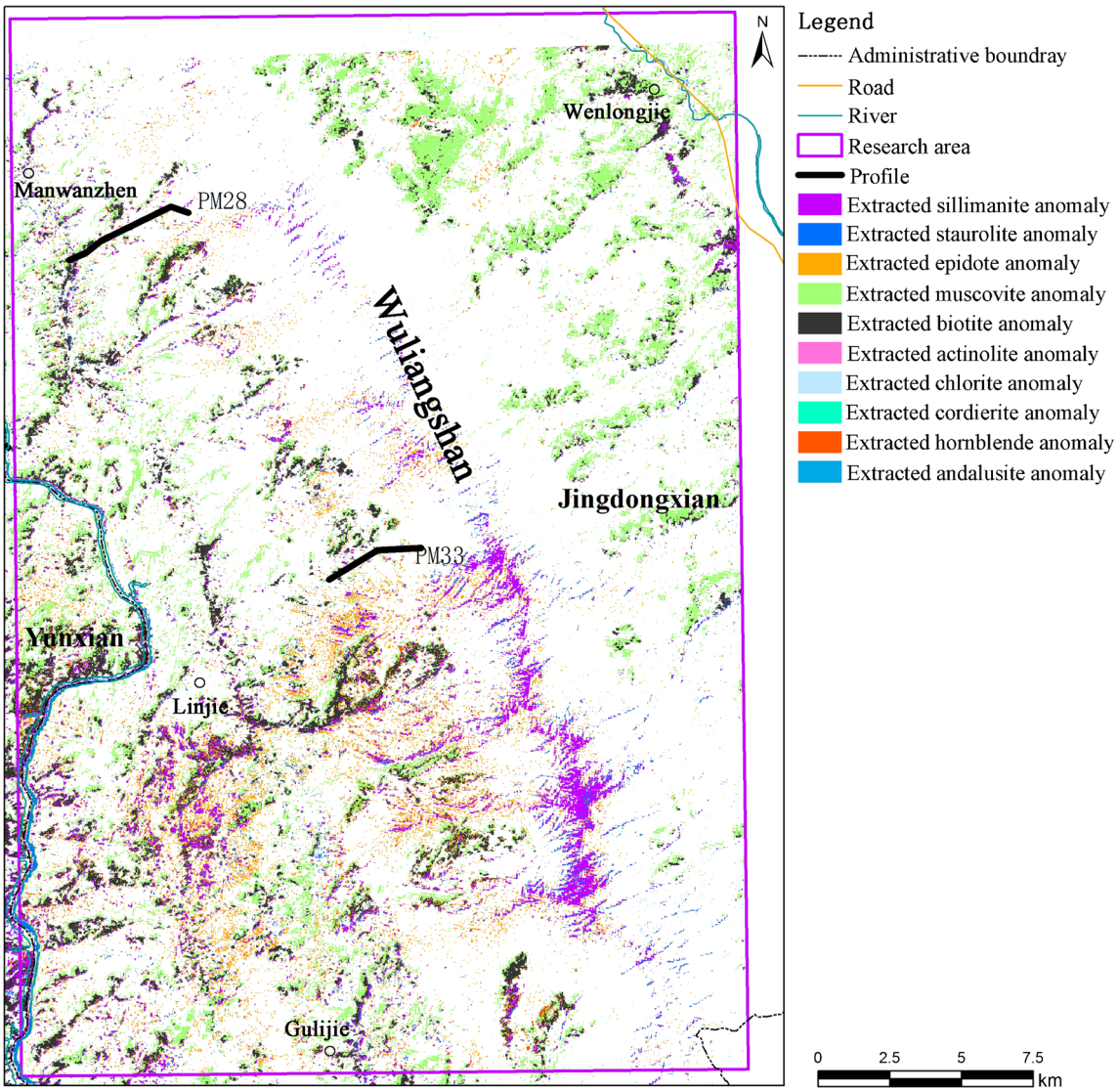

Fig. 8 Distribution map of extracted metamorphic minerals

Table 4 Petrographic analysis of thin sections

Point 88-2 in Profile 33				Point 93-2 in Profile 33			Point 88-2 in Profile 33		
Feature		Granularity (mm)	Percentage (%)	Composition	Granularity (mm)	Percentage (%)	Composition	Granularity (mm)	Percentage (%)
Composition									
Essential minerals	Quartz	≤0.2	40	Quartz	≤1.2	55	Quartz	≤0.3	63
Secondary minerals	Biotite	≤0.5	30	Muscovite	≤0.3	20	Biotite	≤0.5	18
	Epidote	≤0.60	12	Anorthose	≤0.15	10	Muscovite	≤0.3	12
	Scapolite	≤4	10	Biotite	≤0.25	7	Staurolite	≤0.4	5
	Anorthose	≤0.15	8	Kyanite	≤0.7	5	Kyanite	≤0.5	2
	Muscovite	≤0.25	Less	Sillimanite	≤0.15	3	Anorthose	≤0.15	Less
Auxiliary minerals	Metallic mineral	≤0.1	Less	Metallic mineral	≤0.1	Less	Zircon	≤0.05	Less
	Schorlite	≤0.25	Less	Schorlite	≤0.15	Less	Tourmaline	≤0.1	Less
Final name	Crystalloblastic mylonitization epidote-scapolite-biotite-quartz schist			Sillimanite-kyanite-biotite-quartz schist			Kyanite-staurolite-biotite-muscovite-quartz schist		

Petrographic analysis

Petrographic analysis is a method to identify minerals and rocks under a microscope. The thin sections are used to analyze the mineral composition and the mineral structure in the minerals or rocks using a microscope. Hence, the minerals or rock types of 216 thin sections were confirmed by petrographic analysis.

Analysis of metamorphic mineral distribution

From the distribution of different metamorphic minerals, three metamorphic degree regions were identified in the study area. That is, a low metamorphic degree region, a medium metamorphic degree region, and a high metamorphic degree region. Furthermore, the difference between these results and the previous studies was studied further, and a new understanding of the background of the study area was obtained.

Results

Analyzing the information on the ten metamorphic mineral anomalies extracted using the aforementioned method (Fig. 8), the rules of the metamorphic mineral distribution become clear: biotite and muscovite are distributed over the whole study area; hornblende, andalusite, actinolite, and cordierite are distributed in the central and southwestern parts of the study area; a large number of epidote and chlorite minerals is distributed in the central part of the study area; and staurolite and sillimanite are widely distributed in the western and southern parts of the study area and concentrated in the central part in a NW-trending direction. That is, the overall trend of the metamorphic degree decreases from the central part to the outer parts in the study area.

The analysis of the extracted metamorphic minerals anomalies was validated by the material of the profile investigation and petrography, which were provided by the Institute of Yunnan Geological Mineral Exploration in cooperation with our research group. A total of 185 of the 216 analysis results of the sample thin sections were identical to the extracted mineral anomaly results. That is, the extraction accuracy reached 85.65%. The epidote, biotite, and muscovite were related to the lower metamorphic degree; staurolite was related to medium metamorphic degree; and sillimanite was related to high metamorphic degree. To verify these metamorphic minerals which were related to the different metamorphic degree, Point 88-2 of profile PM33, Point 99-2 of profile PM33, and Point 11-2 of profile PM28 were selected to introduce the identification of extracted anomaly information and petrographic analysis in detail as follows:

Point 88-2 of profile PM33 has a concentration of extracted epidote and biotite anomaly information; Point 93-2 of profile PM33 has a concentration of extracted sillimanite, muscovite, and biotite anomaly information; Point 11-2 of profile PM28 has a concentration of extracted staurolite, muscovite, and biotite anomaly information. The petrographic analysis results showed that the rock contains epidote and biotite whose contents are 12 and 30% respectively in Point 88-2 of profile PM33; the rock contains sillimanite, muscovite, and biotite whose contents are 3, 20, and 7% respectively in Point 99-2 of profile PM33; the rock contains staurolite, muscovite, and biotite whose contents are 5, 12, and 18% respectively in Point 11-2 of profile PM28. Therefore, the extracted minerals anomalies are identical to the results of the rock-mineral appraisal (Table 4, Figs. 9, 10, 11).

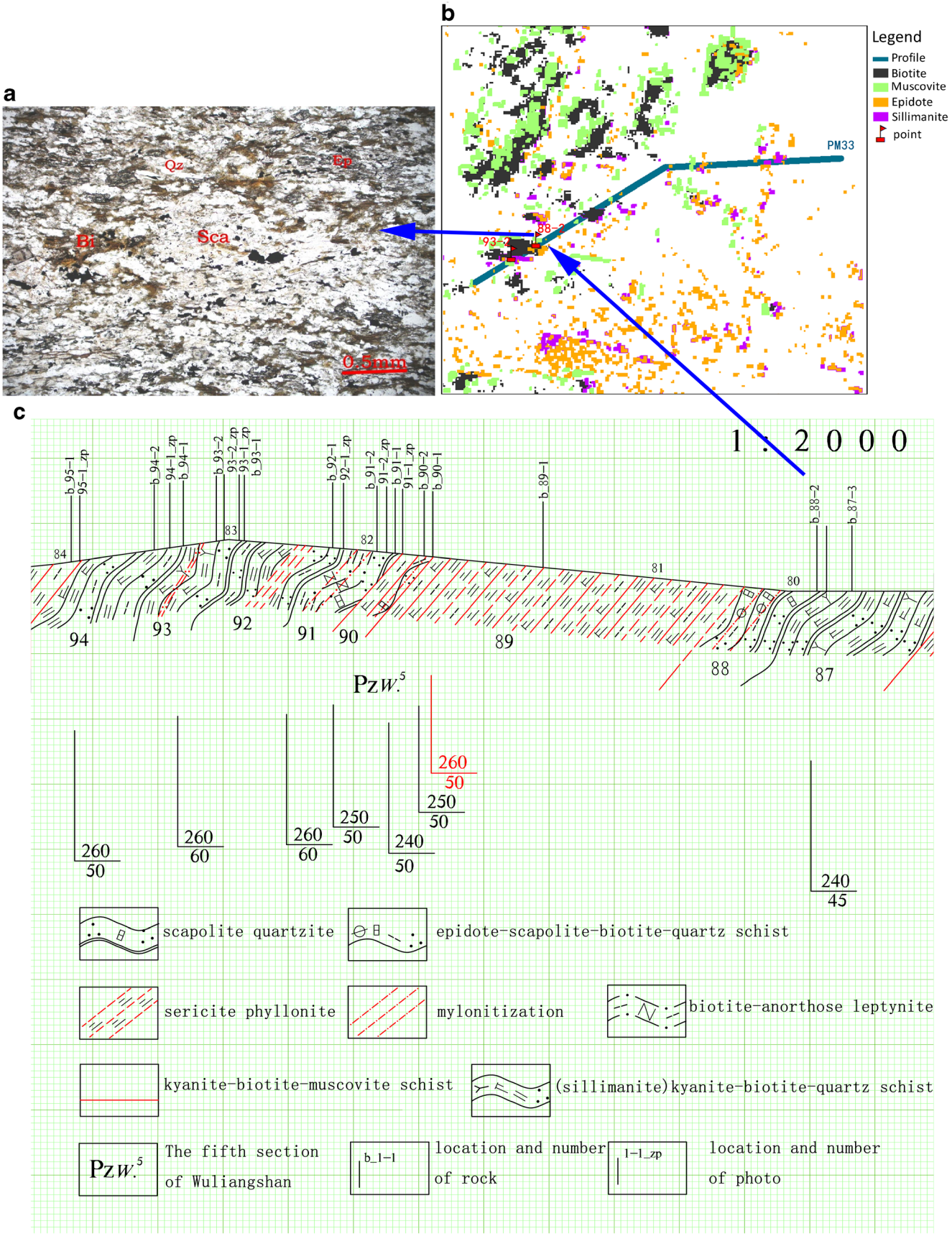

Fig. 9 The verification of point 88-2. **a** PM33-88-2 ⊥ schistosity S, micrograph, single polarization; **b** extracted metamorphic mineral anomaly; **c** profile map of PM33

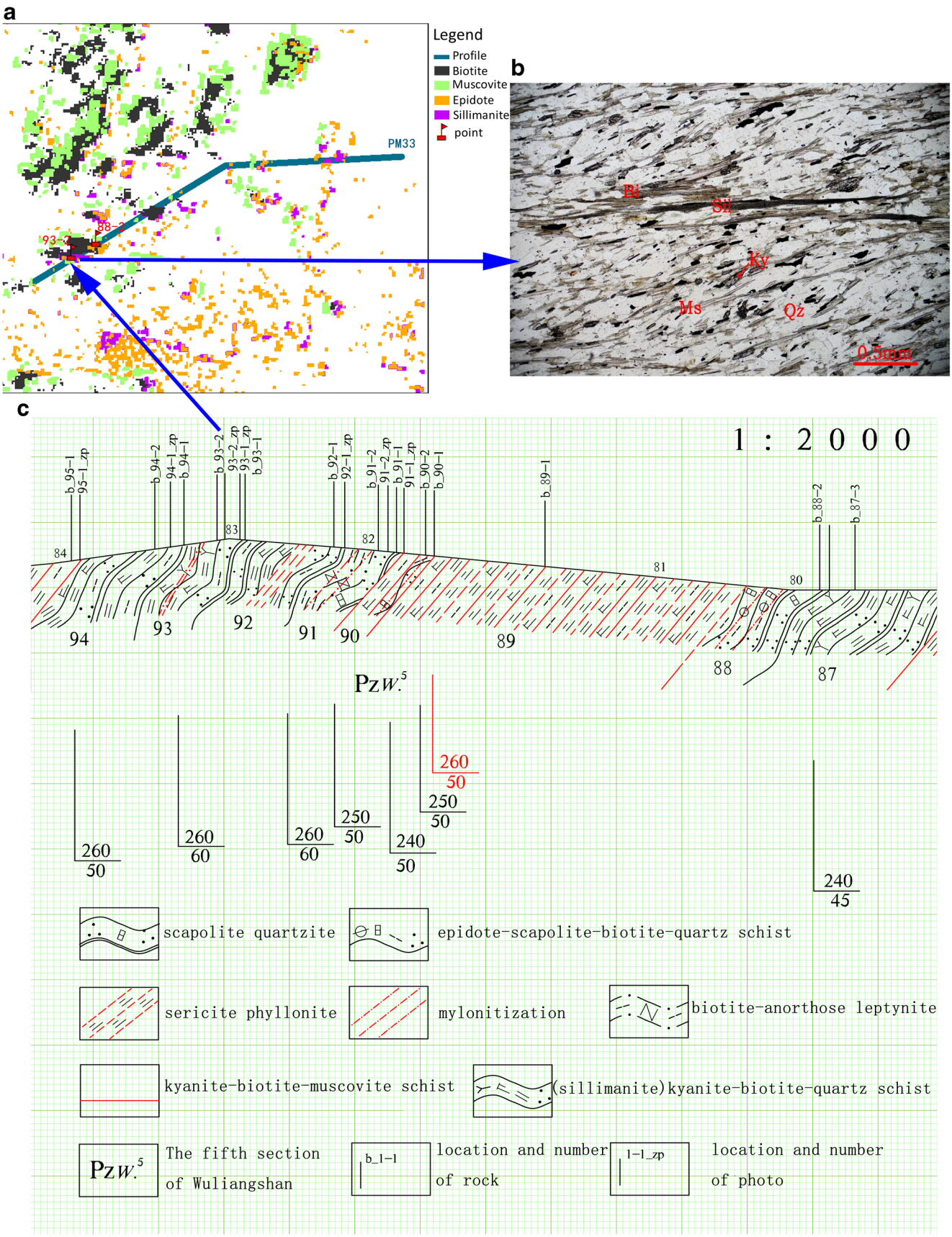

Fig. 10 The verification of point 93-2. **a** Extracted metamorphic minerals; **b** PM33-93-2 ⊥ schistosity S, ∥ lineation L, micrograph, single polarization; **c** profile map of PM33

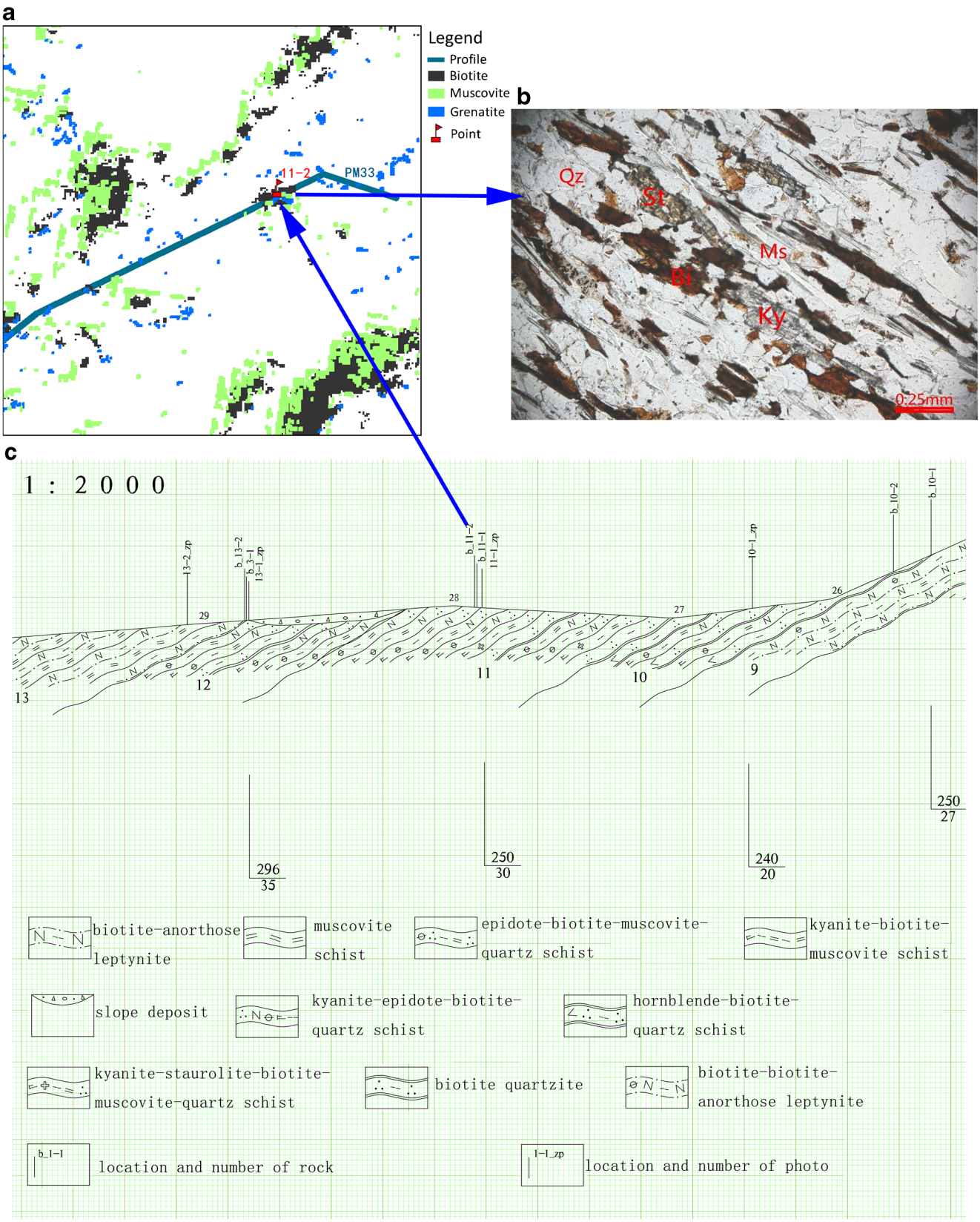

Fig. 11 The verification of point 88-2. **a** Extracted metamorphic minerals; **b** PM28-11-2 ⊥ schistosity S, micrograph, single polarization; **c** profile map PM28

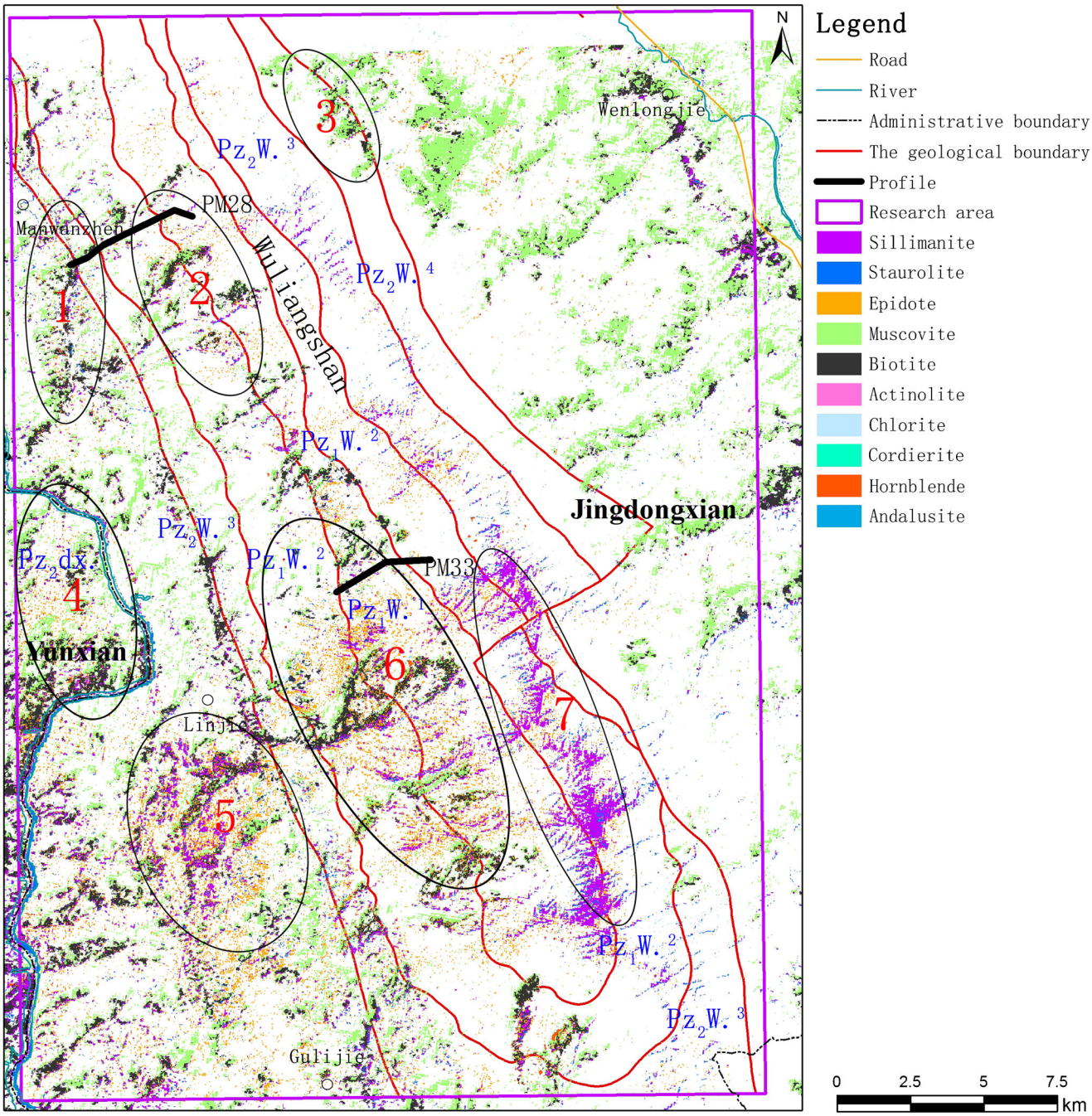

Fig. 12 Analysis of metamorphic regions

Discussion

Previous studies (Yunnan Geological Mineral Bureau, 1990) suggest that the metamorphic degree of the Yunling-Jinghong metamorphic belt is low greenschist facies, the metamorphic degree of sections 1 and 2 is generally high greenschist facies-low amphibolite facies, and the metamorphic degree of sections 3 and 4 is generally low greenschist facies in the Wuliangshan metamorphic belt. Metamorphic minerals such as muscovite, biotite, chlorite, epidote, andalusite, cordierite, staurolite, and kyanite are abundant in the strata of $Pz_1W.^1$ and $Pz_1W.^2$, while muscovite, biotite, chlorite, and epidote are abundant in the strata of $Pz_2dx.$, $Pz_2W.^3$, and $Pz_2W.^4$. The metamorphic degree decreases from the central part to the outer part of the study area.

In this study, seven concentration regions of metamorphic minerals were delineated based on the extracted metamorphic mineral anomalies. The metamorphic mineral anomalies of Region 1 are of muscovite, biotite, and epidote, which indicated that the metamorphic degree is low; the metamorphic

mineral anomalies of Region 2 are of staurolite, muscovite, biotite, and epidote, which indicated that the metamorphic degree is medium; the metamorphic mineral anomalies of Region 3 are of muscovite and biotite, which indicated that metamorphic degree is low; the metamorphic mineral anomalies of Region 4 are of actinolite, muscovite, biotite, epidote, and hornblende, which indicated that metamorphic degree is low-medium; the metamorphic mineral anomalies of Region 5 are of muscovite biotite, chlorite, hornblende, and cordierite, which indicated that metamorphic degree is low-medium; the metamorphic mineral anomalies of Region 6 are of sillimanite, muscovite, biotite, epidote, hornblende, and andalusite, which indicated that metamorphic degree is medium-high; and the metamorphic mineral anomalies of Region 7 are of sillimanite and andalusite, which indicated that metamorphic degree is medium-high (Fig. 12).

Comparing the extracted metamorphic mineral anomalies with previous study results, it can be seen that the overall trend of the metamorphic mineral information is consistent, with some differences. For example, Region 1, related to $Pz_2W.^3$, is of low metamorphic degree; Region 2, related to $Pz_1W.^1$ and $Pz_1W.^2$, is of medium metamorphic degree; Region 3, related to $Pz_2W.^4$, is of low metamorphic degree; Region 4, related to $Pz_2dx.$, is of low metamorphic degree; and Region 6, related to $Pz_1W.^1$ and $Pz_1W.^2$, is of high metamorphic degree. The grade of the metamorphic degree is $6 > 2 > 1 > 4 > 3$, which is consistent with the previous study results that the metamorphic degree decreases from the central part to the outer part of the study area. However, the distribution of the metamorphic mineral anomalies in Region 5 and Region 7 is different from previous study results. Moreover, Region 5 was not recognized as a metamorphic rock region in previous study results, but numerous medium- and high-grade metamorphic mineral anomalies were extracted in this area. The metamorphic degree of Region 7, related to $Pz_1W.^2$ and $Pz_2W.^3$, was recognized as medium-high, but a large amount of sillimanite, which is of high metamorphic degree, was extracted in this region.

Conclusions

In this study, the anomaly information of ten metamorphic minerals, actinolite, chlorite, epidote, biotite, muscovite, hornblende, andalusite, staurolite, cordierite, and sillimanite, was successfully extracted by the PCA and S-A methods based on the multifractal theory with ASTER data in the Wuliangshan area, Yunnan Province, China. Profile investigation and petrographic analysis showed that the identification accuracy of the diagnostic metamorphic minerals reached 85.65%. Therefore, the proposed methods in this study have proven to be valuable for metamorphic minerals anomalies extraction. Meanwhile, based on the extracted metamorphic mineral anomalies, seven concentrations of metamorphic rocks were delineated. Compared with previous studies, the Regions 1, 2, 3, 4, and 6 are consistent with existing data, whereas the Regions 5 and 7 are different, which can provide a useful reference for geological survey in the Wuliangshan area. Further detailed research, particularly on the extracted anomalies, needs to be completed in the future to obtain useful insight for geological mapping and a better understanding of the metamorphic rocks.

Authors' contributions Qi Chen drafted the manuscript and was responsible for the research design, experiments, and analysis. Zhifang Zhao and Qigang Jiang provided technical guidance and reviewed the manuscript. Shucheng Tan provided technical support. Yinggui Tian provided regional geological materials and microscopic analysis data.

Funding information This research received funding by the Natural Science Foundation of China (Project No. 41462015) and the Program of Regional Geology and Mineral Resources Survey (Project No. 12120114060101).

References

Agterberg FP (2012) Multifractals and geostatistics. J Geochem Explor 122:113–122

Agterberg FP (2014) Multifractals and local singularity analysis, Geomathematics: Theoretical Foundations Applications and Future Developments:413–466

Aoki K, Maruyama S, Isozaki Y, Otoh S, Yanai S (2011) Recognition of the Shimanto HP metamorphic belt within the traditional Sanbagawa HP metamorphic belt: new perspectives of the Cretaceous–Paleogene tectonics in Japan. J Asian Earth Sci 42: 355–369

Arnous MO, Sultan YM (2014) Geospatial technology and structural analysis for geological mapping and tectonic evolution of Feiran–Solaf metamorphic complex, South Sinai. Egypt Arabian Journal of Geosciences 7:3023–3049

BaoLong L et al (2008) Zircon SHRIMP dating and its geological implications of the metamorphic rocks in Ailao Shan-Diancang Mountain Ranges, west Yunnan. Acta Petrol Sin 24:2322–2330

Cao L, Cheng Q (2012) Quantification of anisotropic scale invariance of geochemical anomalies associated with Sn-Cu mineralization in Gejiu, Yunan Province, China. J Geochem Explor 122:47–54

Carranza EJM (2009) Geochemical anomaly and mineral prospectivity mapping in GIS. Handbook of Exploration & Environmental Geochemistry 11:890–890

Carranza EJM (2010) Catchment basin modelling of stream sediment anomalies revisited: incorporation of EDA and fractal analysis. Geochemistry Exploration Environment Analysis 10:365–381

Chen G, Cheng Q (2016) Singularity analysis based on wavelet transform of fractal measures for identifying geochemical anomaly in mineral exploration. Comput Geosci 87:56–66

Cheng Q (1999) Multifractality and spatial statistics. Comput Geosci 25: 949–961

Cheng Q (2007) Mapping singularities with stream sediment geochemical data for prediction of undiscovered mineral deposits in Gejiu, Yunnan Province, China. Ore Geol Rev 32:314–324

Cheng Q (2008) Non-linear theory and power-law models for information integration and mineral resources quantitative assessments. Math Geosci 40:503–532

Cheng Q (2012) Singularity theory and methods for mapping geochemical anomalies caused by buried sources and for predicting undiscovered mineral deposits in covered areas. J Geochem Explor 122: 55–70

Cheng Q, Agterberg FP (1996) Multifractal modeling and spatial statistics. Math Geol 28:1–16

Cheng Q, Agterberg FP (2009) Singularity analysis of ore-mineral and toxic trace elements in stream sediments. Comput Geosci 35:234–244

Cheng Q, Agterberg FP, Ballantyne SB (1994) The separation of geochemical anomalies from background by fractal methods. J Geochem Explor 51:109–130

Cheng Q, Xia Q, Li W, Zhang S, Chen Z, Zuo R, Wang W (2010) Density/area power-law models for separating multi-scale anomalies of ore and toxic elements in stream sediments in Gejiu mineral district, Yunnan Province, China. Biogeosciences 7:3019–3025

Cheng Q, Xu Y, Grunsky E (1999) Integrated spatial and spectral analysis for geochemical anomaly separation. In: Lippard SJ, Naess A, Sinding-Larsen R (eds) Proceedings of the International Association for Mathematical Geology Meeting. Trondheim, Norway, pp 87–92

Cheng Q, Xu Y, Grunsky E (2000) Integrated spatial and spectrum method for geochemical anomaly separation. Nat Resour Res 9:43–52

Ferrier G, White K, Griffiths G, Bryant R, Stefouli M (2002) The mapping of hydrothermal alteration zones on the island of Lesvos, Greece using an integrated remote sensing dataset. Int J Remote Sens 23:341–356

Fry N (1984) The field description of metamorphic rocks. Open University Press:588–589

Gabr SS, Hassan SM, Sadek MF (2015) Prospecting for new gold-bearing alteration zones at El-Hoteib area, south Eastern Desert, Egypt, using remote sensing data analysis. Ore Geol Rev 71:1–13

Genyao WU, Jiaju LI (1996) The b_0 values of white micas in metapelites from West Yunnan, China, and their tectono-stratigraphic implications. Geotecton Metallog 20:310–318

Hou Q, Zhong D, Guo Q (2013) Deformation and metamorphism of Wuliangshan area, western Yunnan. Chin J Geochem 48:354–361

JunLai L et al (2006) The dynamic setting and processes of tectonic and magmatic evolution of the oblique collision zone between Indian and Eurasian plates: exemplified by the tectonic evolution of the three river region. eastern Tibet Acta Petrologica Sinica 22:775–786

Kakar MI, Mahmood K, Khan M, Plavsa D (2015) Petrology and geochemistry of amphibolites and greenschists from the metamorphic sole of the Muslim Bagh ophiolite (Pakistan): implications for protolith and ophiolite emplacement. Arab J Geosci 8:6105–6120

Kratt C, Calvin WM, Coolbaugh MF (2010) Mineral mapping in the Pyramid Lake basin: hydrothermal alteration, chemical precipitates and geothermal energy potential. Remote Sens Environ 114:2297–2304

Li C, Ma T, Shi J (2003) Application of a fractal method relating concentrations and distances for separation of geochemical anomalies from background. J Geochem Explor 77:167–175

Lima A, De VB, Cicchella D, Albanese S, Fedele L (2003a) Application of multifractal IDW interpolation and S-A method to determine Pb and U natural background and anomaly values in stream sediments of Campania (Italy). In: European Congress on Regional Geoscientific Cartography and Information Systems

Lima A, Plant JA, Vivo BD, Tarvainen T, Albanese S, Cicchella D (2008) Interpolation methods for geochemical maps: a comparative study using arsenic data from European steam waters. Geochemistry 8: 41–48

Lima A, Vivo BD, Cicchella D, Cortini M, Albanese S (2003b) Multifractal IDW interpolation and fractal filtering method in environmental studies: an application on regional stream sediments of (Italy), Campania region. Appl Geochem 18:1853–1865

Liu Y, Zhou K, Cheng Q (2017) A new method for geochemical anomaly separation based on the distribution patterns of singularity indices. Comput Geosci 105:139–147

Meer FDVD et al (2012) Multi- and hyperspectral geologic remote sensing: a review. Int J Appl Earth Obs Geoinf 14:112–128

Nguyen HC, Jung J, Lee J, Choi SU, Hong SY, Heo J (2015) Optimal atmospheric correction for above-ground forest biomass estimation with the etm+ remote sensor. Sensors 15:18865–18886

Perkins T, Adlergolden S, Berk A, Anderson G, Gardner J, Felde G (2005) retrieval of atmospheric properties from hyper and multispectral imagery with the FLAASH atmospheric correction algorithm. Remote Sensing of Clouds & the Atmosphere X 5979:544–547

Philippon M, Veslud CLCD, Gueydan F, Brun JP, Caumon G (2015) 3D geometrical modelling of post-foliation deformations in metamorphic terrains (Syros, Cyclades, Greece). J Struct Geol 78:134–148

Rani N, Mandl VR, Singh T (2017) Evaluation of atmospheric corrections on hyperspectral data with special reference to mineral mapping. Geosci Front 8:797–808

Rowan LC, Goetz AFH, Ashley RP (1977) Discrimination of hydrothermally altered and unaltered rocks in visible and near infrared multispectral images. Geophysics 42:522–535

Sabins FF (1999) Remote sensing for mineral exploration. Ore Geol Rev 14:157–183

Spalla MI, Di PS, Gosso G, Siletto GB, Bistacchi A (2002) Mapping tectono-metamorphic histories in the Lake Como basement (Southern Alps, Italy). Memorie Di Scienze Geologiche 54:149–167

Wang G, Carranza EJM, Zuo R, Hao Y, du Y, Pang Z, Sun Y, Qu J (2012) Mapping of district-scale potential targets using fractal models. J Geochem Explor 122:34–46

Wang L et al. (2015) Arcuate nappe structure on the region of Huilong Mountains in the northern margin of Wuliang Mountains in western Yunnan. Chinese Journal of Geology

Xu Y, Cheng Q (2001) A fractal filtering technique for processing regional geochemical maps for mineral exploration. Geochemistry Exploration Environment Analysis 1:147–156

Xue X (1988) A probe on the formation mechanism of wuliangshan-yingpanshan metamorphic belt. Yunnan Geology 7:303–399

Yunnan Geological Mineral Bureau (1990) Regional geology of Yunnan Province. Geological Publishing House, Beijing

Zoheir B, Emam A (2014) Field and ASTER imagery data for the setting of gold mineralization in Western Allaqi–Heiani belt, Egypt: a case study from the Haimur deposit. J Afr Earth Sci 99:150–164

Zuo R, Carranza EJM, Cheng Q (2012) Fractal/multifractal modelling of geochemical exploration data. J Geochem Explor 122:1–3

Zuo R, Xia Q, Wang H (2013a) Compositional data analysis in the study of integrated geochemical anomalies associated with mineralization. Appl Geochem 28:202–211

Zuo R, Xia Q, Zhang D (2013b) A comparison study of the C–A and S–A models with singularity analysis to identify geochemical anomalies in covered areas. Appl Geochem 33:165–172